

This is the accepted manuscript made available via CHORUS. The article has been published as:

## Complete $\beta$ -decay pattern for the high-priority decay-heat isotopes $^{137}\text{I}$ and $^{137}\text{Xe}$ determined using total absorption spectroscopy

B. C. Rasco, K. P. Rykaczewski, A. Fijałkowska, M. Karny, M. Wolińska-Cichocka, R. K. Grzywacz, C. J. Gross, D. W. Stracener, E. F. Zganjar, J. C. Blackmon, N. T. Brewer, K. C. Goetz, J. W. Johnson, C. U. Jost, J. H. Hamilton, K. Miernik, M. Madurga, D. Miller, S. Padgett, S. V. Paulauskas, A. V. Ramayya, and E. H. Spejewski

Phys. Rev. C **95**, 054328 — Published 31 May 2017

DOI: [10.1103/PhysRevC.95.054328](https://doi.org/10.1103/PhysRevC.95.054328)

# Complete $\beta$ -Decay Pattern for the High-Priority Decay-Heat Isotopes $^{137}\text{I}$ and $^{137}\text{Xe}$ Determined Using Total Absorption Spectroscopy

B.C. Rasco,<sup>1,2,3,4,\*</sup> K.P. Rykaczewski,<sup>2</sup> A. Fijałkowska,<sup>5,3</sup> M. Karny,<sup>5,2,1</sup> M. Wolińska-Cichońska,<sup>6,2,1</sup>  
R.K. Grzywacz,<sup>3,2,1</sup> C.J. Gross,<sup>2</sup> D.W. Stracener,<sup>2</sup> E.F. Zganjar,<sup>4</sup> J.C. Blackmon,<sup>4</sup> N.T.  
Brewer,<sup>1,2,3</sup> K.C. Goetz,<sup>7,3</sup> J.W. Johnson,<sup>2</sup> C.U. Jost,<sup>2</sup> J.H. Hamilton,<sup>8</sup> K. Miernik,<sup>5</sup> M.  
Madurga,<sup>3</sup> D. Miller,<sup>3,9</sup> S. Padgett,<sup>3</sup> S.V. Paulauskas,<sup>3</sup> A.V. Ramayya,<sup>8</sup> and E.H. Spejewski<sup>2</sup>

<sup>1</sup>JINPA, Oak Ridge National Laboratory, Oak Ridge, Tennessee 37831, USA

<sup>2</sup>Physics Division, Oak Ridge National Laboratory, Oak Ridge, TN 37831, USA

<sup>3</sup>Dept. of Physics and Astronomy, University of Tennessee, Knoxville, TN 37966, USA

<sup>4</sup>Dept. of Physics and Astronomy, Louisiana State University, Baton Rouge, LA 70803 USA

<sup>5</sup>Faculty of Physics, University of Warsaw, Pasteura 5, PL-02-093 Warszawa, Poland

<sup>6</sup>Heavy Ion Laboratory, University of Warsaw, PL-02-093 Warszawa, Poland

<sup>7</sup>CIRE Bredesen Center, University of Tennessee, Knoxville, TN 37966, USA

<sup>8</sup>Dept. of Physics and Astronomy, Vanderbilt University, Nashville, TN 37212, USA

<sup>9</sup>Chemical and Radiation Measurements Department,  
Idaho National Laboratory, Idaho Falls, ID 83415, USA

(Dated: May 4, 2017)

**Background** An assessment done under the auspices of the Nuclear Energy Agency in 2007 suggested that the  $\beta$  decays of abundant fission products in nuclear reactors may be incomplete. Many of the nuclei are potentially affected by the so called Pandemonium effect and their  $\beta$ - $\gamma$  decay heat should be restudied using the total absorption technique. The fission products  $^{137}\text{I}$  and  $^{137}\text{Xe}$  were assigned highest priority for restudy due to their large cumulative fission branching fractions. In addition, measuring  $\beta$ -delayed neutron emission probabilities is challenging and any new technique for measuring the  $\beta$ -neutron spectrum and the  $\beta$ -delayed neutron emission probabilities is an important addition to nuclear physics experimental techniques.

**Purpose** To obtain the complete  $\beta$ -decay pattern of  $^{137}\text{I}$  and  $^{137}\text{Xe}$  and determine their consequences for reactor decay heat and  $\bar{\nu}_e$  emission. Complete  $\beta$ -decay feeding includes ground state to ground state  $\beta$  feeding with no associated  $\gamma$  rays, ground state to excited states  $\beta$  transitions followed by  $\gamma$  transitions to the daughter nucleus ground state, and  $\beta$ -delayed neutron emission from the daughter nucleus in the case of  $^{137}\text{I}$ .

**Method** We measured the complete  $\beta$ -decay intensities of  $^{137}\text{I}$  and  $^{137}\text{Xe}$  with the Modular Total Absorption Spectrometer at Oak Ridge National Laboratory. We describe a novel technique for measuring the  $\beta$ -delayed neutron energy spectrum, which also provides a measurement of the  $\beta$ -neutron branching ratio,  $P_n$ .

**Results** We validate the current ENSDF evaluation of  $^{137}\text{Xe}$   $\beta$  decay. We find that major changes to the current ENSDF assessment of  $^{137}\text{I}$   $\beta$ -decay intensity are required. The average  $\gamma$  energy per  $\beta$  decay for  $^{137}\text{I}$   $\beta$  decay ( $\gamma$  decay heat) increases by 19%, from 1050 keV to 1250 keV, which increases the average  $\gamma$  energy per  $^{235}\text{U}$  fission by 0.11%. We measure a  $\beta$  delayed neutron branching fraction for  $^{137}\text{I}$   $\beta$  decay of  $7.9 \pm 0.2(\text{fit}) \pm 0.4(\text{sys})\%$  and we provide a  $\beta$ -neutron energy spectrum.

**Conclusions** The Modular Total Absorption Spectrometer measurements of  $^{137}\text{I}$  and  $^{137}\text{Xe}$  demonstrate the importance of revisiting and remeasuring complex  $\beta$  decaying fission products with total absorption spectroscopy. We demonstrate the ability of the Modular Total Absorption Spectrometer to measure  $\beta$ -delayed neutron energy spectra.

## I. INTRODUCTION

The  $\beta$  decays of the isotopes  $^{137}\text{Xe}$  [ $T_{1/2}=229.1(8)$  s,  $Q_\beta=4162(3)$  keV] and  $^{137}\text{I}$  [ $T_{1/2}=24.5(2)$  s,  $Q_\beta=6027(8)$ ] seem to be well studied in terms of high energy resolution  $\gamma$  spectroscopy [1, 2]. However, the assessment of fission-decay products by the Nuclear Energy Agency (NEA) of the Organization for Economic Cooperation and Development [3] has encouraged a re-exploration of many isotopes due to a possible systematic bias of the earlier studies based on low efficiency detectors known as the Pandemonium effect [4]. Total absorption spectroscopy

(TAS) is a solution to the Pandemonium effect, as was shown in the fiducial TAS work on fission products performed by Greenwood in the 1990s [5] and by other TAS groups [6–9]. In the NEA report,  $^{137}\text{Xe}$  and  $^{137}\text{I}$  are classified as priority 1 nuclei for reactor decay heat measurements. Incomplete data on many of these high priority nuclei may be responsible for the recently reported reactor antineutrino anomaly [3, 9, 10]. The nuclei  $^{137}\text{Xe}$  and  $^{137}\text{I}$ , produced with cumulative yields of 6.1% and 3.0% for  $^{235}\text{U}$  thermal neutron fission respectively [11], contribute substantially to the overall reactor antineutrino flux, so their decay properties can affect the magnitude of the reactor  $\bar{\nu}_e$  anomaly.

$^{137}\text{I}$  is a well studied  $\beta$ -neutron emitter, and as such it is interesting to examine the  $\beta$ -neutron decay component using total absorption spectrometry. Understanding  $\beta$ -neutron emission is critical for operation and further

---

\*Electronic address: [brasco@utk.edu](mailto:brasco@utk.edu)

development of nuclear power reactors. By exploiting properties of the Modular Total Absorption Spectrometer (MTAS), we demonstrate a novel way to measure  $\beta$ -delayed neutron energy spectra. By measuring both the  $\beta$ - $\gamma$  and the  $\beta$ -delayed neutron components of the complete  $\beta$ -decay intensity with MTAS, it is possible to obtain complete  $\beta$ -decay feeding patterns with a single instrument. By performing these measurements with a single detector within one experiment, accurate simultaneous measurements of  $P_n$  and  $\beta$ -neutron energy spectra for unknown nuclei are possible. We demonstrate these abilities by measuring the  $\beta$ -delayed neutron energy spectrum of  $^{137}\text{I}$ .

## II. EXPERIMENTAL TECHNIQUE

The  $\beta$  decays of mass  $A = 137$  isotones  $^{137}\text{I}$  and  $^{137}\text{Xe}$  were measured with MTAS at Oak Ridge National Laboratory. MTAS consists of 19 hexagonal NaI(Tl) crystals forming a  $4\pi$ -array [8, 12, 13]. There is approximately 1000 kg of NaI(Tl) detector material in MTAS, covering over 99% of the solid angle around the measured activities. The  $\gamma$ -ray efficiency for full  $\gamma$ -ray energy absorption in on-line conditions is a nearly flat 81% from 300 keV to 800 keV, and then drops smoothly to 72% at 5 MeV [8]. At the center of MTAS there are two 1 mm thick silicon detectors, each with 7 segments, that are used as  $\beta$ -triggers. The segmentation of the silicon detectors is used to monitor the position of the implanted tape activity. The silicon detectors suppress laboratory background by at least three orders of magnitude. In addition to the active background suppression, there are over 5000 kg of lead shielding around MTAS.

The two activities were produced by inducing fission in a  $\text{UC}_x$  target with a 40 MeV, 50 pA proton beam. The  $^{137}\text{I}$  isotope was extracted, ionized with a surface-ionization source, accelerated to 40 keV, and analyzed by means of an on-line separator with a mass resolution of  $M/\Delta M = 600$  [14]. The radioactive beam was collected on a transport tape, which was moved into MTAS, measured, and then transported away afterwards to prevent buildup of the associated long-lived daughter activities. For  $^{137}\text{Xe}$  [ $T_{1/2}=229.1(8)$  s] measurements, ions were collected for 60.0 sec, then the tape was paused for 4.0 minutes to allow the  $^{137}\text{I}$  to decay away, and then the remaining ions on the tape were transported into the MTAS detector and measured for 8.0 minutes. For  $^{137}\text{I}$  [ $T_{1/2}=24.5(2)$  s], the ions were collected for 15.0 sec, then the tape was paused for 15.0 sec to reduce the counting rate, and then the ions on the tape were transported into the MTAS detector and measured for 50.0 sec.

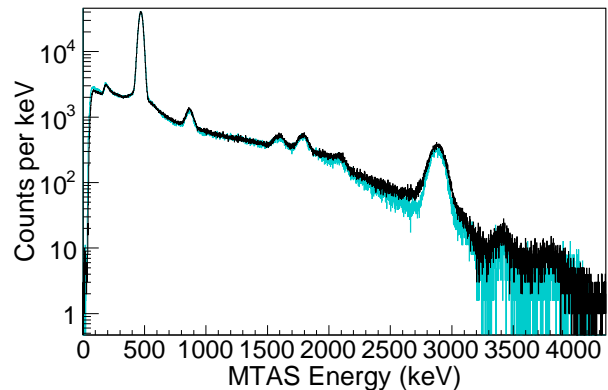


FIG. 1: (Color online) Background subtracted  $^{137}\text{Xe}$  MTAS energy spectrum (black) compared to the simulated MTAS response based on the ENSDF data (cyan). For  $^{137}\text{Xe}$ ,  $Q_\beta$  is 4162(3) keV.

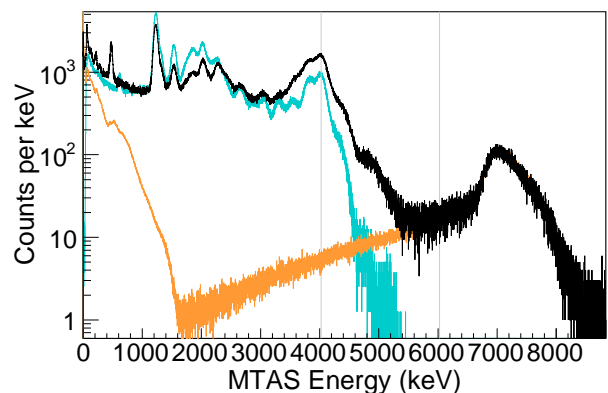


FIG. 2: (Color online) Background subtracted  $^{137}\text{I}$  MTAS energy spectrum (black) compared to the simulated MTAS response based on the ENSDF data (cyan) and the fit neutron spectrum (orange). The large peak beginning around 6850 keV is a sum of the  $^{127}\text{I}$  and  $^{23}\text{Na}$  neutron capture peaks and the fast neutron energies. For  $^{137}\text{I}$ ,  $Q_\beta$  is 6027(8) and the neutron separation energy,  $S_n$ , is 4025.56(10) keV, which are shown in gray.

## III. ANALYSIS

### A. MTAS Data Versus Simulated ENSDF Spectra

The comparison of the simulated ENSDF data and the raw  $\beta$ -triggered MTAS data for  $^{137}\text{Xe}$  is shown in Fig. 1. The relatively good agreement of the ENSDF data with the raw MTAS data can be considered as a validation of the  $^{137}\text{Xe}$  ENSDF  $\beta$ -feeding intensities.

For  $^{137}\text{I}$ , the simulated ENSDF data does not agree well with the MTAS data, see Fig. 2. There are two regions of interest in the histogram, the  $\beta$ - $\gamma$  decays to the  $^{137}\text{Xe}$  ground state which is seen below  $\sim 5500$  keV and the  $\beta$ -delayed neutrons which leave a clear signature in MTAS above 6700 keV.

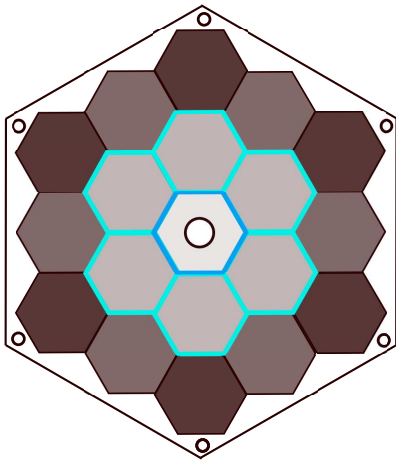


FIG. 3: (Color online) The MTAS detector is organized into rings based on distance from the center of MTAS. The holed center module is outlined in dark blue, the 6 modules of the inner ring are outlined in light blue, the 6 modules of the middle ring are shown in a middle gray, and the 6 modules of the outer ring are shown in a darker grey.

### B. Modularity, Decay Paths, and Efficiency

A schematic picture of MTAS is shown in Fig. 3. The MTAS modules are organized into rings based on distance from where the implanted tape source is located in the center of MTAS and are all 21" long. This is an effective way to organize the MTAS modules in order to evaluate the various spectra [8, 12, 13, 15]. In addition to organizing data there are several uses of the modularity of MTAS. First, an obvious increase in efficiency as a function of mass can be observed as a function of the number of rings summed together. Second, the individual decay paths from the fed energy levels can be evaluated by comparing energy deposits in different rings and modules. Both of these abilities demonstrate the power of a large modular detector.

It is interesting to compare the change in efficiency versus the mass of NaI in the detector. We show plots of the center module energy (blue), the sum of the center module and the inner ring of modules energy (red), and the total MTAS energy (black) spectra in Fig. 4. Fig. 4 shows how structures detected by total absorption spectroscopy emerge as the mass of the detector increases. Even with detailed knowledge of the individual decay paths, it would be very challenging to evaluate the  $\beta$ -decay feeding pattern from just the center module alone. It is easier to correctly evaluate the center module plus the inner module, and is even easier with all of the modules of MTAS. Evaluating the neutron peak is more straight forward with all of the MTAS modules than just the center module and inner ring. Including all of the MTAS modules increases the neutron capture efficiency by a factor of 2. It would be very difficult to evaluate neutron spectra with a detector made of only a single,

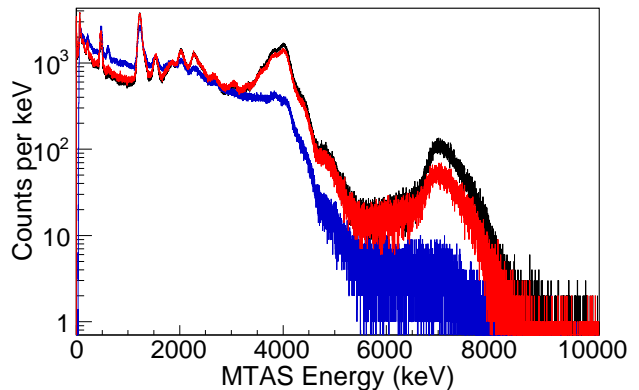


FIG. 4: (Color online)  $^{137}\text{I}$  ( $^{137}\text{Xe}$  daughter subtracted) data for center module energy (blue), center plus inner ring energy (red), and the total MTAS spectrum (black). The total MTAS neutron efficiency doubles, when compared to the center module plus inner ring neutron signal efficiency. There are 17% additional  $\gamma$  counts between 3500 and 4500 keV in the total MTAS spectrum when compared to the center plus inner ring spectrum alone.

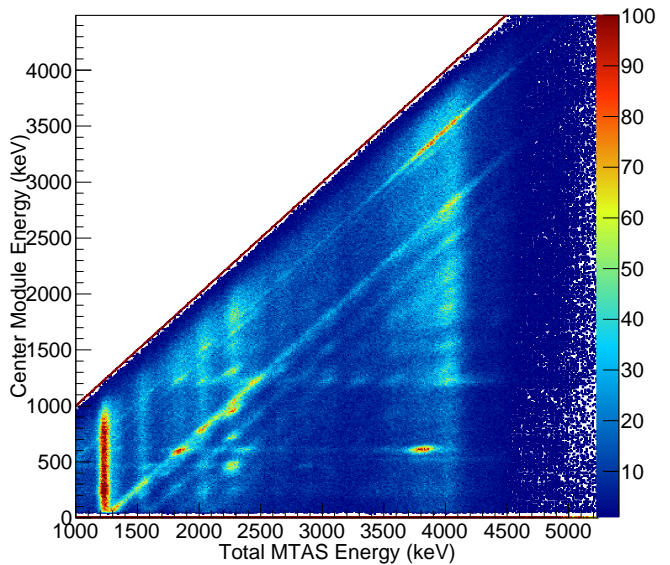


FIG. 5: (Color online)  $^{137}\text{I}$  center module energy versus the total MTAS energy spectrum. The z scale is linear. The spectrum is cut at 1 MeV to remove the large peaks from  $^{137}\text{Xe}$  daughter activity, this activity is shown in Fig. 6.

even if large, center-like module. The evaluation of the neutron-capture peak is discussed in detail below.

Another use of MTAS's modularity is that it can disentangle the major decay paths from a given level. The 2D plot of the center module versus the total MTAS energy for the  $^{137}\text{I}$  data is shown in Fig. 5. As a rule of thumb, when compared with the total MTAS energy spectrum, the center module spectrum highlights individual lower

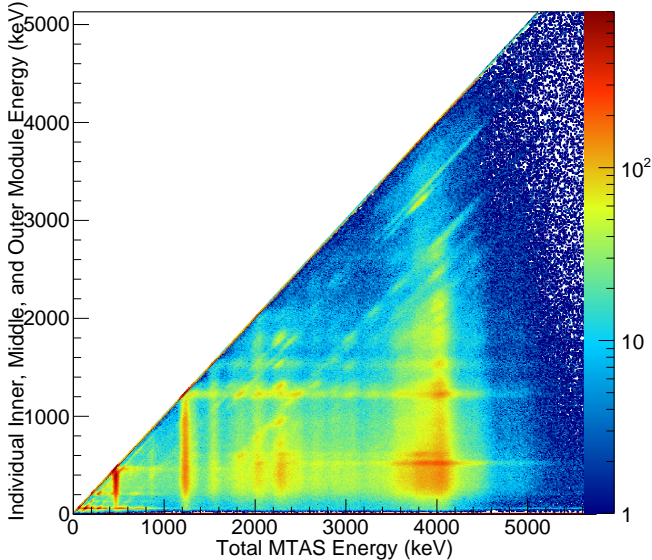


FIG. 6: (Color online)  $^{137}\text{I}$  individual module energy versus the total MTAS energy spectrum. The z scale is logarithmic. Just above the x axis the 58 keV  $\gamma$  from  $^{127}\text{I}(n, n'\gamma)^{127}\text{I}$  can be seen in all of the MTAS modules and the  $^{137}\text{Xe}$  daughter decays at 455 and 849 keV can be seen.

energy ( $<1$  MeV)  $\gamma$  rays and the sums of multiple  $\gamma$ -ray decays.

The 2D plot of the individual inner, middle, and outer modules versus total MTAS energy for the  $^{137}\text{I}$  data is shown in Fig. 6. Plotting the individual inner, middle, and outer single modules versus the total MTAS energy highlights individual higher ( $>1$  MeV) energy  $\gamma$ -rays.

We show the most likely decay paths from levels in the 3970 to 4020 keV bin by taking cuts on the total energy detected in MTAS in Fig. 5 and 6 and plotting what the individual modules detect. An example of the individual  $\gamma$  rays detected from the decay from levels in a particular energy bin are labeled and shown in Fig. 7. We fit each major total MTAS energy bin with the  $\gamma$  rays from various decay paths and thereby estimate the fraction for each decay path [13].

### C. $\beta$ -Delayed Neutrons

There are two requirements for a NaI detector to efficiently detect neutrons and measure their kinetic energy. There must be enough NaI to thermalize the neutrons in a reasonably fast time and there must be enough NaI surrounding the neutron capture location to detect the resulting cascade of  $\gamma$  rays from neutron capture. Fast neutrons are emitted from the center of a total absorption detector, while capture events are located somewhere off-center in the detector. If the capture events are near the edge of the total absorption spectrometer the probability

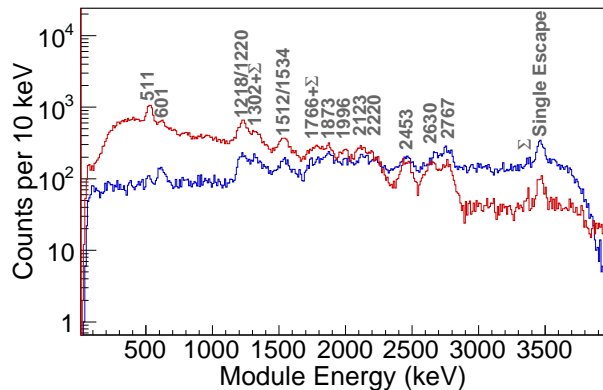


FIG. 7: (Color online) Plot for  $^{137}\text{I}$  of the individual MTAS modules with a cut on the total MTAS energy between 3970 and 4020 keV. The center module is shown in blue and all other modules are shown in red. Individual  $\gamma$  rays known from high precision measurements are identified. Summation peaks are labeled with a  $\Sigma$ .

of detecting all of the neutron capture  $\gamma$  rays is reduced and therefore the efficiency of that detector as a neutron spectrometer is reduced. The very large MTAS has both of these required properties and therefore can serve as a good neutron detector.

$^{127}\text{I}$  and  $^{23}\text{Na}$  in NaI have many low-lying states through which neutrons with a wide range of energies can lose large amounts of energy and thermalize quickly through  $(n, n'\gamma)$  interactions. The main processes of neutron energy loss are from  $^{127}\text{I}(n, n'\gamma)^{127}\text{I}$  reactions and some  $^{23}\text{Na}(n, n'\gamma)^{23}\text{Na}$ . There is also s-wave scattering without  $\gamma$  emission. However, given the much heavier  $^{127}\text{I}$  and  $^{23}\text{Na}$ , it takes many more s-wave collisions, and hence more time, to slow down than from  $(n, n'\gamma)$  interactions.

The  $\gamma$  rays from the  $(n, n'\gamma)$  reactions are detected throughout MTAS. The most clear signature of neutrons in NaI that we observe is an asymmetric 58 keV  $^{127}\text{I}(n, n'\gamma)^{127}\text{I}$  peak, which is detected in all modules of MTAS when fast neutrons are present. There is effectively zero probability to detect a 58 keV  $\gamma$  ray that is emitted from the center of MTAS in the inner, middle, or outer rings of MTAS. Therefore detecting 58 keV  $\gamma$  rays in all MTAS modules is a unique signal that there are scattered fast neutrons present.

The neutron separation energy,  $S_n$ , for  $^{128}\text{I}$  is 6.826 MeV and for  $^{24}\text{Na}$   $S_n$  is 6.959 MeV. The thermal capture cross sections for  $^{127}\text{I}$  and  $^{23}\text{Na}$  are 6.146 b and 0.528 b respectively, so the neutron-capture spectra are dominated by capture on  $^{127}\text{I}$ . By measuring the background spectrum we measure the average  $S_n$  energy of thermal background neutrons for NaI, which is used to calibrate the neutron capture peak. In addition to a calibration point, we use the resolution of the background thermal neutron capture peak to estimate the neutron energy resolution. During MTAS experiments, we ran every tenth

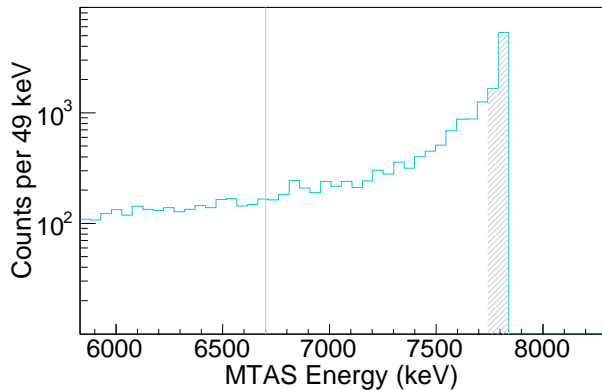


FIG. 8: (Color online) The high energy range of the simulated MTAS response to 1 MeV neutrons is shown in blue. This response function does not include the MTAS energy resolution, which is taken into account during MTAS spectra analysis. The grey line is the cutoff energy for counts that are part of the 'MTAS NaI neutron capture efficiency',  $\epsilon_n^{MTAS}$ . The hatched area represents the 'peak neutron efficiency' for this response function. The efficiencies of the auxiliary  $\beta$  detectors are not included in this illustration.

tape cycle as a background cycle, with protons on  $UC_x$  target, but with no activity deposited on tape and with the same tape movement cycle. The full width half maximum (FWHM) of the capture peak of background thermal neutrons is 250 keV and we therefore expect our  $\beta$ -neutron energy spectrum to have a similar resolution.

If the entire neutron capture energy is detected, it is summed with the  $\gamma$  energies of the  $(n, n'\gamma)$  and other neutron interactions in MTAS. This wide capture peak is a clear signal that neutrons are present. By subtracting the average  $S_n$ , which is obtained from the measurement of background thermal neutrons, we fit and extract the neutron energy spectrum. In the case of  $^{137}\text{I}$  the neutron energy spectrum and the  $\beta$ -delayed neutron feeding are the same, since the  $Q_{\beta} - S_n$  window suppresses feeding to the excited levels of  $^{136}\text{Xe}$ . For many decays this is not the case, the neutron will decay to an excited level in the daughter nucleus and will decay with an additional  $\gamma$  ray.

There are two characteristics that represent the neutron efficiency of MTAS and both characteristics are based on GEANT4 simulations of the MTAS response to mono-energetic neutrons. The characteristic efficiencies are guided by considering the shape of the response function and therefore it is useful to examine a typical MTAS response function. The higher energy portion of the MTAS response function to 1 MeV neutron is shown in Fig. 8.

The overall shape of the response function and the shape of the response function that influences the data fitting can be represented by quoting two different efficiency characterizations. The first characterization is based on the full energy deposit efficiency of the mono-energetic neutrons and is labeled as the 'peak neutron efficiency'. This efficiency represents fast neutrons events

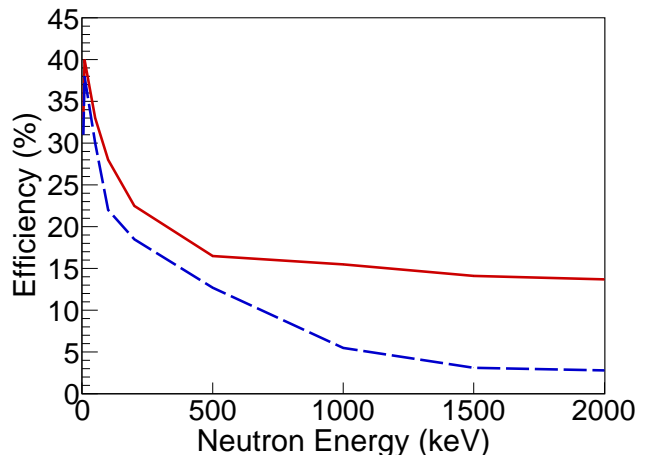


FIG. 9: (Color online) The 'MTAS NaI neutron capture efficiency',  $\epsilon_n^{MTAS}$ , (solid, red) and the 'peak neutron efficiency' (blue, dashed) from simulations of MTAS. The efficiency of the auxiliary  $\beta$  detectors are not included in the neutron efficiency calculations. Further detail of each efficiency curve is provided in the text.

that deposit all initial kinetic energy and all of the NaI neutron capture energy in MTAS. The second characterization, called the 'MTAS NaI neutron capture efficiency' and represented by  $\epsilon_n^{MTAS}$ , is based on the number of fast neutrons that deposit energy above the NaI neutron capture peak energy. This efficiency represents partial neutron kinetic energy deposits and/or partially collected  $\gamma$  rays from the neutron capture process. The neutron response functions all have a tail below the neutron full energy deposit (including the neutron capture energy).  $\epsilon_n^{MTAS}$  includes the statistics in the tail of the response function above the  $^{127}\text{I}$  and  $^{23}\text{Na}$  neutron capture energies.  $\epsilon_n^{MTAS}$  is a more useful measure of the MTAS neutron efficiency because the entire part of the response function above the NaI neutron capture energy is used during the deconvolution (fitting) process. Plots of both MTAS efficiency characterizations versus energy are shown in Fig. 9. The neutron response functions (after applying the detector resolution and auxiliary detector cuts) that are fit to the  $^{137}\text{I}$   $\beta$ -delayed neutron data are shown in Fig. 10.

As was recently demonstrated in [16, 17], if the neutron efficiency has a large dependence on the neutron energy and/or the  $\beta^-$  energy, this leads to challenges measuring the neutron branching fraction,  $P_n$ , for detectors with efficiencies that depend on energy but do not measure the energy directly. MTAS detects neutrons and their energy, hence MTAS data can be used to calculate the total number of neutrons detected. By comparing the total number of neutrons measured with the total number of ground and excited state  $\beta$ -decay feedings we calculate

$$P_n = \frac{N_{\beta n}}{(N_{\beta\gamma} + N_{\beta n})}, \quad (1)$$

where  $N_{\beta n}$  is the calculated number of  $\beta$ -decay neutron events that decay to the ground state of  $^{136}\text{Xe}$  and  $N_{\beta\gamma}$  is the calculated number of  $\beta$ -decay events that populate states in  $^{137}\text{Xe}$  and decay to the ground state of  $^{137}\text{Xe}$ .

We calculate an uncertainty in the total number of neutron events by propagating uncertainties of detector thresholds, the variance of  $\epsilon_n^{MTAS}$  over each neutron energy bin, and an inherent systematic uncertainty of the neutron simulations by neutron energy of 5% per bin. The detector thresholds uncertainties have minimal influence on the error until the highest neutron energies measured and therefore have negligible impact on the total neutron number uncertainty. The simulation uncertainty is based on the magnitude of recent corrections to the low energy neutron modeling in GEANT4 [18]. This results in a 5% systematic relative uncertainty in the total number of neutron events and its respective influence on the  $P_n$  value. From fitting of the entire neutron capture spectrum, which includes the detector energy resolution, we obtain a 5% error in the total number of neutron events. For GEANT4  $\beta$  and  $\gamma$  simulations we set this systematic uncertainty at 2% [9]. The energy-dependent efficiency of the MTAS  $\beta$  detectors is included in the simulations. We report the estimated simulation error in the final numbers as the dominant systematic error.

For  $\beta$ -decay events that eventually decay to the  $^{137}\text{Xe}$  ground state,  $N_{\beta\gamma}$ , we calculate that  $N_{\beta\gamma} = (6.488 \pm 0.016(stat) \pm 0.13(sys)) \times 10^6$  events. For  $N_{\beta n}$ , the number of events that emit a  $\beta$  delayed neutron and decay to the  $^{136}\text{Xe}$  ground state, we calculate  $(0.559 \pm 0.003(stat) \pm 0.03(sys)) \times 10^6$  events. The total number of events include events that leave no signal in MTAS, but are included in the response function [8, 13]. Using these numbers to calculate the delayed neutron branching value, we get  $P_n = 7.9 \pm 0.2(fit) \pm 0.4(sys)\%$ . The total uncertainties are dominated by the assumed simulation systematic uncertainties.

The MTAS capture peak neutron spectrum and the fit of the simulation by bins is shown in Fig. 10. The neutron energy spectrum calculated from the fit in Fig. 10 is shown in Fig. 11. There are some minor differences between the ENSDF and our calculation. This difference occurs mostly in the lowest energy bin, where MTAS is highly sensitive to low energy neutrons. Our coincidence time window of 500 ns is long enough for 1 keV neutrons to travel into MTAS, thermalize, and be captured. This neutron energy threshold is extremely low. The energy resolution is consistent with the 250 keV FWHM estimate of the neutron energy uncertainty.

## IV. RESULTS

### A. $^{137}\text{Xe}$ Complete $\beta$ -Feeding Intensity

The  $^{137}\text{Xe}$  complete  $\beta$ -feeding intensity is shown in Fig. 12. Since the ground state and the first-excited state  $\beta$  feedings are 98% of the complete  $\beta$ -decay intensity,

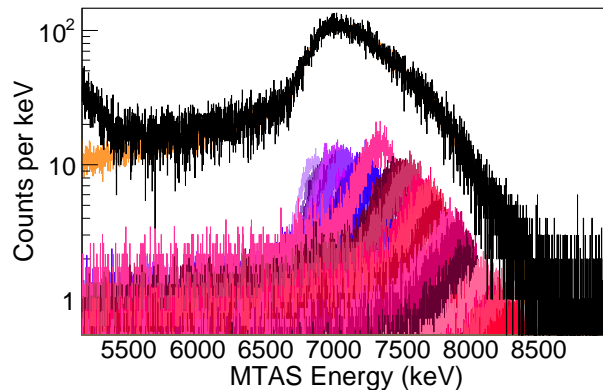


FIG. 10: (Color online)  $^{137}\text{I}$  total MTAS data is shown in black, simulated individual neutron response functions are shown in various reds, and the sum of the neutron simulations is shown in orange.

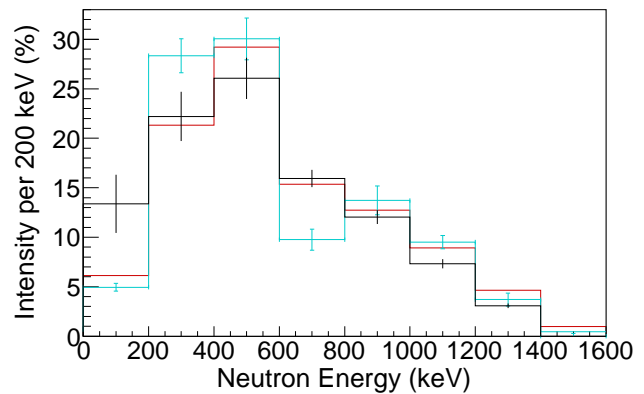


FIG. 11: (Color online) The  $^{137}\text{I}$   $\beta$ -delayed neutron energy spectrum from MTAS (black) and from ENSDF [2] (cyan and red). There are two different histograms based on the same ENSDF data shown. The first histogram (cyan) is the ENSDF data binned into 200 keV bins with uncertainties shown for the feedings to all levels within the bin. The second histogram (red) is the ENSDF data convoluted with a 250 keV full-width half-maximum Gaussian and then binned into 200 keV energy bins. The convolution emulates the energy resolution of MTAS. The error bars for the convoluted ENSDF spectrum are similar to the binned ENSDF data and are not shown in order to preserve clarity.

our results should be considered as a validation of the current ENSDF evaluation, with only minor changes to the higher energy level  $\beta$  feeding and slightly more precise main branching ratios.

### B. $^{137}\text{I}$ Complete $\beta$ -Feeding Intensity

The  $^{137}\text{I}$   $\beta$  and  $\beta$ - $\gamma$ -feeding intensity is shown in Fig. 13. We have used the known level scheme from high precision experiments up to 4100 keV, just above the neu-

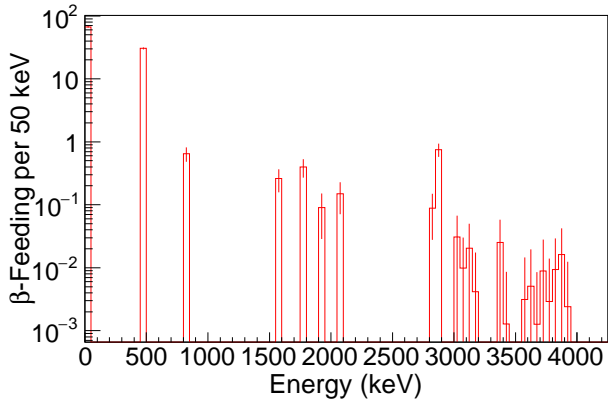


FIG. 12: (Color online)  $^{137}\text{Xe}$  complete  $\beta$ -feeding intensity (red). The  $\beta$  feeding to the ground state is  $67 \pm 2\%$  and the  $\beta$  feeding to the first excited state (455 keV) is  $31 \pm 1\%$ . The current ENSDF value of the  $\beta$  feeding to the ground state is  $67 \pm 3\%$  and the  $\beta$  feeding to the first excited state is  $31 \pm 3\%$  [2].

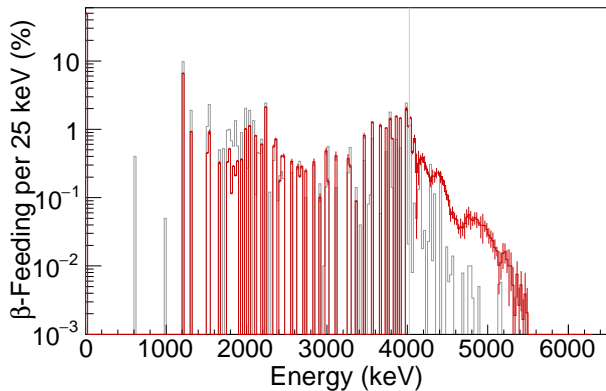


FIG. 13: (Color online)  $^{137}\text{I}$   $\beta$ - $\gamma$  feeding intensity for MTAS (red) and ENSDF (gray) [2]. By using 25 keV bins we do not imply a 25 keV resolution.  $S_n$  is shown as a gray vertical line. Above 5500 keV the measurements are statistically consistent with zero feeding.

tron separation energy. Above this energy we have partitioned the energy into 25 keV bins. This arbitrary dividing point was chosen because there are not enough known levels to fit the measured data above 4100 keV. Compared to the ENSDF  $\beta$ -feeding data there are many more  $\gamma$  rays measured by MTAS in the continuously binned region above  $S_n$  energy than previously reported.

The  $^{137}\text{I}$  complete  $\beta$ -feeding intensity is shown in Fig. 14. The  $^{137}\text{I}$   $\beta$ -feeding intensity is made up of three main components, the ground state feeding (which comes with no  $\gamma$  rays), the  $\beta$  feeding to excited levels that de-excite via  $\gamma$  rays, and the decays to levels that de-excite via neutron emission to the ground state in the  $^{136}\text{Xe}$  nucleus. It is expected that there is little  $\beta$ -neutron feeding to the first excited  $2^+$  state in the  $N = 82$   $^{136}\text{Xe}$  due to its high energy of 1313 keV ( $Q_\beta - S_n = 2002$  keV). We

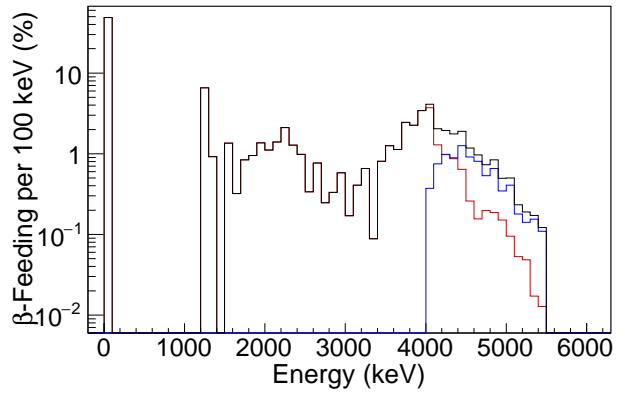


FIG. 14: (Color online)  $^{137}\text{I}$  complete  $\beta$ -feeding intensity (black),  $\beta$ - $\gamma$  (red), and  $\beta$ -delayed neutron feeding (blue). The energy is partitioned into 100 keV bins, which is a compromise between the 25 keV bins used in the  $\beta$ - $\gamma$  calculation and the 200 keV bins used in the  $\beta$ -delayed neutron calculations. Above 5500 keV the measurements are consistent with zero feeding.

validate that there is no  $\beta$ -neutron feeding to the first excited state, as we detect no 1313 keV  $\gamma$  rays in the center module in coincidence with the neutron spectrum. The ability of MTAS to detect the  $\beta$ -neutron feeding to excited states is described in [8]. As described above, the MTAS setup detects all three of these components of the  $\beta$  feeding. It is not clear how the ground state  $\beta$ -feeding nor the uncertainty of the previous measurement of 45.2(7)% was made [1, 19].

After applying time cuts to minimize contamination, we calculate a total of  $(7.047 \pm 0.016(stat) \pm 0.14(sys)) \times 10^6$   $\beta$ -decay events and  $(0.559 \pm 0.003(stat) \pm 0.03(sys)) \times 10^6$   $\beta$ -delayed neutron events. A ground state  $\beta$  feeding of  $49 \pm 1\%$  is measured. When compared to the ENSDF  $^{137}\text{I}$  data, the average  $\gamma$  energy per  $\beta$  decay increases by 19%, from 1050 keV to 1250 keV. The measured  $\beta$ -feeding intensity at the neutron separation energy increases by a factor 2 and above the neutron separation energy it increases by 5 times, when compared to the ENSDF assessment. By integrating the binned  $\beta$ -feeding intensity it is calculated that a total of  $8.3 \pm 1.0\%$  of the  $\gamma$  intensity is above the neutron separation threshold. This gives a  $\beta$ -decay neutron branch,  $P_n$ , of  $7.9 \pm 0.2(fit) \pm 0.4(sys)\%$ . This is in agreement with the recent  $P_n$  result of  $7.74 \pm 0.14\%$  [16] obtained by the BELEN collaboration and is on the higher side when compared with the current ENSDF value of  $7.0 \pm 0.5\%$  [1, 2] or the recent evaluation  $7.22 \pm 0.21\%$  [20]. Our results have two major improvements over previous  $P_n$  measurements. First we have an extremely low energy neutron detection threshold. And second, we use our improved, simultaneously measured,  $\beta$ - $\gamma$  intensity measurement. The total amount of decays from above the neutron separation energy are split approximately equal between  $\gamma$  decay to the  $^{137}\text{Xe}$

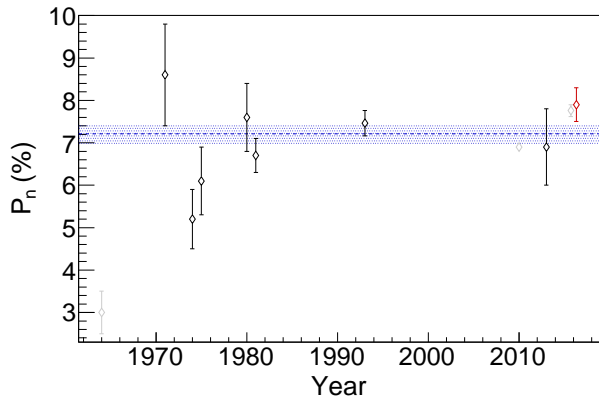


FIG. 15: (Color online) Measured  $^{137}\text{I}$  neutron branching ratios,  $P_n$ , versus year. A weighted average for  $P_n$  using values before 2016 [20] is shown as the dashed blue line and the current results are shown in red. The 2010 experiment is a preliminary result and it has no error bars. Measurements used to calculate the average are shown in black and other measurements not used to calculate the weighted average are shown in gray.

ground state and by neutron emission. The measured value of the  $\beta$ -delayed neutron branching has varied over time, as shown in Fig. 15. We note that the  $P_n$  for  $^{137}\text{I}$  is considered to be well known [20]. However systematic uncertainties, sometimes not included in the results, dominate this  $P_n$  value [21]. Therefore the assessment of the  $P_n$  value may have a somewhat subjective accuracy.

### C. Impact on Decay Heat and $\bar{\nu}_e$ Flux

The average  $\gamma$  energy for  $^{137}\text{I}$  decay measured with MTAS increases by 19% when compared to the ENSDF data [2] and by 10% when compared to the ENDF/B-VII.1 data (ENDF) [22]. The different results reflect different content in the ENSDF and ENDF databases.

The  $\gamma$ -decay heat is defined [3] as

$$H_\gamma(t) = \sum_i \lambda_i N_i(t) \bar{E}_{i,\gamma}, \quad (2)$$

where  $\lambda_i$  is the total decay constant of nuclei of type  $i$ ,  $N_i(t)$  is the number of nuclei of type  $i$  at time  $t$ ,  $\bar{E}_{i,\gamma}$  is the average  $\gamma$  energy emitted per  $\beta$  decay by nuclei of type  $i$ , and the sum is over all fission product nuclei. In Fig. 16 we plot the ratio of the  $\gamma$ -decay heat per  $^{235}\text{U}$  fission obtained using the MTAS  $\beta$  feeding for  $^{137}\text{I}$  to the calculated values based on either the ENSDF data or the ENDF data. The plotted results are consistent given that the average ENDF  $\gamma$  energy is 1130 keV, the average ENSDF  $\gamma$  energy is 1050 keV, and the average MTAS  $\gamma$  energy is 1250 keV. These changes imply an increase in  $\gamma$  energy per  $^{235}\text{U}$  fission decay of 0.11% when compared with the ENSDF data and of 0.06% when compared with the ENDF data.

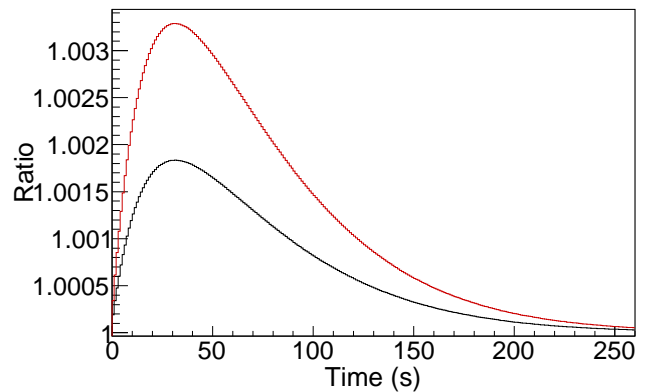


FIG. 16: (Color online) Ratio of the MTAS measured  $\gamma$  decay heat to calculated  $\gamma$  decay heat for  $n_{th} + ^{235}\text{U}$ . The two curves are based on two different data sets, the bottom curve (black) is the change compared to the ENDF data and the top curve (red) is compared to the ENSDF data for  $^{137}\text{I}$  and ENDF data for all other decays.

The average  $\beta$  energy decreases by 4%, from 1950 keV to 1870 keV and the average  $\bar{\nu}_e$  energy decreases by 4%, from 2520 keV to 2430 keV, when compared to the ENSDF evaluation of  $^{137}\text{I}$ . The number of  $\bar{\nu}_e$  emitted from  $^{137}\text{I}$  and detected by an inverse  $\beta$ -decay (IBD)  $\bar{\nu}_e$  detector is reduced by 5%. The influence on  $\bar{\nu}_e$  emission during  $^{137}\text{I}$   $\beta$  decay of the MTAS changes to the ENSDF data set are two fold, the ground state feeding goes up and the emitted  $\gamma$  energy also goes up. The former increases the average  $\bar{\nu}_e$  energy while the latter decreases the average  $\bar{\nu}_e$  energy. The changes of  $\beta$  feeding to higher energy levels in  $^{137}\text{Xe}$  are larger than the change of the feeding to the ground state, with a net effect that decreases both the average  $\bar{\nu}_e$  energy and the number of IBD  $\bar{\nu}_e$  detected.

## V. CONCLUSIONS

We measure the complete  $\beta$ -feeding intensities for two NEA priority 1 nuclei using MTAS. For  $^{137}\text{Xe}$ , we obtain slightly more precise main branching fractions and validate the current ENSDF assessment. For  $^{137}\text{I}$ , we find larger changes are needed to correct the ENSDF  $\beta$ -feeding assignments. The ground-state feeding increases from  $45.2 \pm 0.7\%$  to  $49 \pm 1\%$ . The  $\gamma$ -decay component after  $^{137}\text{I}$   $\beta$  decay increases by at least a factor of 2 near the neutron separation energy and the  $\gamma$ -decay component after  $^{137}\text{I}$   $\beta$  decay increases by up to 5 times or more at 1 MeV above the neutron separation energy. The average  $\gamma$  energy per  $\beta$  decay increases by 19%, from 1050 keV to 1250 keV, when compared to the current ENSDF data and increases by 10%, from 1130 keV to 1250 keV, when compared with the current ENDF data. These corrections imply an increase in  $\gamma$  energy per  $^{235}\text{U}$  fission decay of 0.11% when compared with the current ENSDF data

and of 0.06% when compared with the current ENDF data.

The MTAS result for the neutron branching ratio,  $P_n = 7.9 \pm 0.2(\text{fit}) \pm 0.4(\text{sys})\%$ , is on the high side of previous measurements, but is within  $2\sigma$  of the recommended neutron branching ratio [20]. The MTAS neutron energy spectrum measurement at low neutron energy yields higher intensity than in the ENSDF evaluation, which could be explained by the low energy threshold for neutron detection in MTAS. However, the overall  $\beta$ -delayed neutron energy spectrum is in line with current  $\beta$ -neutron energies above 200 keV.

In addition to improved measurement of multi- $\gamma$ -ray events when compared to low-efficiency  $\gamma$  detectors, MTAS measures ground state to ground state feeding, and it is a  $\beta$ -neutron spectrometer. These capabilities make MTAS a unique detector which measures the complete  $\beta$ -decay patterns of very neutron rich nuclei.

## Acknowledgments

We would like to thank the ORNL Tandem operations staff for providing the excellent quality proton beams necessary for this work. This research was also sponsored by the Office of Nuclear Physics, U. S. Department of Energy under contracts DE-AC05-00OR22725 (ORNL), DE-FG02-96ER40983 (UTK), DE-FG02-96ER40978 (LSU), DE-FG02-96ER41006 (MSU), DE-FG-05-88ER40407 (VU), UMO-2013/08/T/ST2/00624 and UMO-2015/18/E/ST2/00217 from the Polish National Centre for Science. This work was also supported and inspired by the IAEA Coordinated Research Project for a "Reference Database for  $\beta$ -Delayed Neutron Emission".

- 
- [1] E. Browne and J. Tuli, Nuclear Data Sheets **108**, 2173 (2007), ISSN 0090-3752, URL <http://www.sciencedirect.com/science/article/pii/S0090375207000804>.
- [2] URL <http://www.nndc.bnl.gov/ensdf/>.
- [3] T. Yoshida and A. L. Nichols, *Assessment of Fission Product Decay Data for Decay Heat Calculations: A report by the Working Party on International Evaluation Co-operation of the Nuclear Energy Agency Nuclear Science Committee* (Nuclear Energy Agency, Organization for Economic Co-operation and Development, Paris, France, 2007), ISBN 9789264990340.
- [4] J. C. Hardy, L. C. Carraz, B. Jonson, and P. G. Hansen, Phys. Lett. B **71**, 307 (1977).
- [5] R. Greenwood, R. Helmer, M. Putnam, and K. Watts, Nuclear Instruments and Methods in Physics Research Section A: Accelerators, Spectrometers, Detectors and Associated Equipment **390**, 95 (1997), ISSN 0168-9002, URL <http://www.sciencedirect.com/science/article/pii/S0168900297003562>.
- [6] A. Algora, D. Jordan, J. L. Taín, B. Rubio, J. Agramunt, A. B. Perez-Cerdan, F. Molina, L. Caballero, E. Nácher, A. Krasznahorkay, et al., Phys. Rev. Lett. **105**, 202501 (2010), URL <http://link.aps.org/doi/10.1103/PhysRevLett.105.202501>.
- [7] A.-A. Zakari-Issoufou, M. Fallot, A. Porta, A. Algora, J. L. Taín, E. Valencia, S. Rice, V. M. Bui, S. Cormon, M. Estienne, et al. (IGISOL collaboration), Phys. Rev. Lett. **115**, 102503 (2015), URL <http://link.aps.org/doi/10.1103/PhysRevLett.115.102503>.
- [8] M. Karny, K. P. Rykaczewski, A. Fijałkowska, B. C. Rasco, M. Wolińska-Cichočka, R. K. Grzywacz, K. C. Goetz, D. Miller, and E. F. Zganjar, Nuclear Instruments and Methods in Physics Research Section A: Accelerators, Spectrometers, Detectors and Associated Equipment **836**, 83 (2016), ISSN 0168-9002, URL <http://www.sciencedirect.com/science/article/pii/S0168900216308646>.
- [9] B. C. Rasco, M. Wolińska-Cichočka, A. Fijałkowska, K. P. Rykaczewski, M. Karny, R. K. Grzywacz, K. C. Goetz, C. J. Gross, D. W. Stracener, E. F. Zganjar, et al., Phys. Rev. Lett. **117**, 092501 (2016), URL <http://link.aps.org/doi/10.1103/PhysRevLett.117.092501>.
- [10] A. A. Sonzogni, T. D. Johnson, and E. A. McCutchan, Phys. Rev. C **91**, 011301 (2015), URL <http://link.aps.org/doi/10.1103/PhysRevC.91.011301>.
- [11] Katakura, Jun-ichi, Minato, Futoshi, and Ohgama, Kazuya, EPJ Web of Conferences **111**, 08004 (2016), URL <http://dx.doi.org/10.1051/epjconf/201611108004>.
- [12] B. C. Rasco, A. Fijałkowska, M. Karny, K. P. Rykaczewski, M. Wolińska-Cichočka, R. Grzywacz, and K. C. Goetz, Nuclear Instruments and Methods in Physics Research Section A: Accelerators, Spectrometers, Detectors and Associated Equipment **788**, 137 (2015), ISSN 0168-9002, URL <http://www.sciencedirect.com/science/article/pii/S0168900215004519>.
- [13] B. C. Rasco, A. Fijałkowska, M. Karny, K. Rykaczewski, M. Wolińska-Cichočka, K. C. Goetz, R. K. Grzywacz, C. J. Gross, K. Miernik, and S. V. Paulauskas, JPS Conf. Proc. **6**, 107 (2015), URL <http://journals.jps.jp/doi/abs/10.7566/JPSCP.6.030018>.
- [14] D. Stracener, Nuclear Instruments and Methods in Physics Research Section B: Beam Interactions with Materials and Atoms **204**, 42 (2003), ISSN 0168-583X, 14th International Conference on Electromagnetic Isotope Separators and Techniques Related to their Applications, URL <http://www.sciencedirect.com/science/article/pii/S0168583X02018888>.
- [15] M. Wolińska-Cichočka, K. P. Rykaczewski, A. Fijałkowska, M. Karny, R. K. Grzywacz, C. J. Gross, J. W. Johnson, B. C. Rasco, and E. F. Zganjar, Nuclear Data Sheets **120**, 22 (2014), ISSN 0090-3752, URL <http://www.sciencedirect.com/science/article/pii/S0090375214004487>.
- [16] J. Agramunt, J. Taín, M. Gómez-Hornillos, A. Garcia, F. Albiol, A. Algora, R. Caballero-Folch, F. Calviño, D. Cano-Ott, G. Cortés, et al., Nuclear Instruments and Methods in Physics Research Section A: Accelerators, Spectrometers, Detectors and As-

- sociated Equipment **807**, 69 (2016), ISSN 0168-9002, URL <http://www.sciencedirect.com/science/article/pii/S0168900215013169>.
- [17] M. Madurga, S. V. Paulauskas, R. Grzywacz, D. Miller, D. W. Bardayan, J. C. Batchelder, N. T. Brewer, J. A. Cizewski, A. Fijałkowska, C. J. Gross, et al., Phys. Rev. Lett. **117**, 092502 (2016), URL <http://link.aps.org/doi/10.1103/PhysRevLett.117.092502>.
- [18] A. R. García, E. Mendoza, and D. Cano-Ott, *Validation of the thermal neutron physics in geant4*, URL <https://indico.cern.ch/event/245281/>.
- [19] B. Fogelberg and H. Tovedal, Nuclear Physics A **345**, 13 (1980), ISSN 0375-9474, URL <http://www.sciencedirect.com/science/article/pii/0375947480904108>.
- [20] B. Singh, Private Communication, to be publish in Nuclear Data Sheets (2017).
- [21] L. Mathieu, O. Serot, T. Materna, A. Bail, U. Köster, H. Faust, O. Litaize, E. Dupont, C. Jouanne, A. Letourneau, et al., Journal of Instrumentation **7**, P08029 (2012), URL <http://stacks.iop.org/1748-0221/7/i=08/a=P08029>.
- [22] M. Chadwick, M. Herman, P. Obloinsk, M. Dunn, Y. Danon, A. Kahler, D. Smith, B. Pritychenko, G. Arbanas, R. Arcilla, et al., Nuclear Data Sheets **112**, 2887 (2011), ISSN 0090-3752, special Issue on ENDF/B-VII.1 Library, URL <http://www.sciencedirect.com/science/article/pii/S009037521100113X>.